ICARUS **131,** 4–14 (1998)
ARTICLE NO. IS975815

Shape of Asteroid 433 Eros from Inversion of Goldstone Radar Doppler Spectra

David L. Mitchell

Jet Propulsion Laboratory, California Institute of Technology, Pasadena, California 91109
E-mail: mitchell@think.jpl.nasa.gov

R. Scott Hudson

School of Electrical Engineering and Computer Science, Washington State University, Pullman, Washington 99164

and

Steven J. Ostro and Keith D. Rosema

Jet Propulsion Laboratory, California Institute of Technology, Pasadena, California 91109

Received May 31, 1996; revised April 21, 1997

We use new analysis techniques to constrain the shape of 433 Eros with Goldstone radar data obtained during the asteroid's close approach in 1975. A previous analysis of these data (Ostro, Rosema, and Jurgens, 1990, *Icarus* 84, 334–351) used estimates of the echo's spectral edge frequencies as a function of asteroid rotation phase to constrain the convex envelope of Eros' pole-on silhouette. Our approach makes use of the echo's full Doppler-frequency distribution (effectively ~15 times more echo data points) and is thus capable of constraining shape characteristics, such as concavities, within this convex envelope. The radar echoes are weak and north-south ambiguous, which limits the accuracy of our models. We present two different approaches, perturbations to an ellipsoid and successive approximations, that help to quantify the model uncertainties and identify features that are likely to be real. Both approaches yield models that are tapered along their lengths, with one or more prominent concavities on one side but not the other. We do not have sufficient information to determine the exact nature of the concavities, and in particular, whether they are craters, troughs, or bends in Eros' overall shape. The pole-on silhouette of the successive approximation model is shaped like a kidney bean, which resembles a nearly pole-on optical image derived from speckle interferometry (Drummond and Hege, 1989, in *Asteroids II* (R. P. Binzell, T. Gehrels, and M. S. Matthews, Eds.), pp. 171–191, Univ. of Arizona Press, Tucson); however, we cannot exclude shapes, such as the perturbation model, with more than one large concavity. Variations in the pyroxene/olivine ratio over Eros' surface have been inferred from visual and infrared observations (Murchie and Pieters, 1996, *J. Geophys. Res.* 101, 2201–2214). Correlating these variations with our shape information, we find that the side with concavities is relatively px-rich compared with the more rounded opposing side. © 1998 Academic Press

Key Words: **asteroid; radar; 433 Eros; shape; NEAR.**

INTRODUCTION

Asteroid 433 Eros is the second largest member of the near-Earth population and also one of the most elongated. Only the Earth-crosser 1620 Geographos, roughly one-tenth the size of Eros, is known to be more elongated (Ostro *et al.* 1995). Much of our current knowledge of Eros is based on extensive observations made when the asteroid passed within 0.15 AU of Earth in 1975 (Zellner 1975). Initial results from those observations were reported in a special issue of *Icarus* (Vol. 28, 1976).

Eros' visual lightcurves have amplitudes as large as 1.5 magnitudes, with two distinct maxima and two distinct minima, which occur in the order Max 1, Min 1, Max 2, Min 2, in the convention of Millis *et al.* (1976). During the 1975 apparition, Max 1 was the brighter, or primary, maximum for solar phase angles less than about 40°. Several lightcurve analyses have yielded estimates of Eros' pole direction and elongation in the context of axisymmetric models (Magnusson 1989 and references therein). Eros' elongation is also evident in 3.5-cm Goldstone radar echoes (Jurgens and Goldstein 1976); as the asteroid rotates, the echo's Doppler bandwidth varies by about a factor of two. A consensus model ellipsoid (Zellner 1976), based primarily on the 1975 lightcurve and radar observations, has dimensions $36 \times 15 \times 13$ km and a pole direction within a few degrees of ecliptic coordinates $\lambda = 16°$ and $\beta = +11°$.

The 1976 consensus ellipsoid provides a reasonable first approximation to Eros' shape, but it is known to be simplistic. Jurgens and Goldstein (1976; hereafter JG76) noted that asymmetries in the echo's frequency distribution at

0019-1035/98 $25.00

minimum-bandwidth (end-on) rotation phases indicated ''a difference in surface reflectivity or surface slopes on opposite sides of the asteroid.'' A nonaxisymmetric shape is also evident from the unequal maxima and unequal minima in Eros' lightcurves.

Clues to the nature of the asymmetries noted by Jurgens and Goldstein can be obtained from the echo bandwidth as a function of rotation phase. Ostro *et al.* (1990; hereafter ORJ90) used estimates of the edge frequencies as a function of rotation phase to constrain the convex envelope, or ''hull,'' of Eros' pole-on silhouette and to determine a correction to the Doppler ephemeris of Eros' center of mass during the 1975 radar observations. They found that Eros' hull is shaped like a rounded trapezoid, which helps to explain odd harmonics observed in both the radar spectra and optical lightcurves. Interestingly, the hull's center of figure does not coincide with its center of rotation, suggesting a nonuniform distribution of mass projected onto the convex hull, which could, for example, result from concavities along the hull's long, flat side (ORJ90).

The NEAR spacecraft will rendezvous with Eros in February, 1999, and measure the asteroid's size, shape, mass, spin, and magnetic field, as well as its surface composition and geology (Santo *et al.* 1995). Detailed shape information based on spacecraft images and ground-based radar images have opened the way to realistic studies that address the physics of impacts on irregularly shaped asteroids (Greenberg *et al.* 1994, Asphaug *et al.* 1996) as well as orbital dynamics and ejecta placement in a weak and complicated gravity field (Geissler *et al.* 1996, Scheeres *et al.* 1996). Existing Eros radar data are not strong enough to permit a unique, three-dimensional shape reconstruction, such as those obtained for the near-Earth asteroids 4769 Castalia and 4179 Toutatis (Hudson and Ostro 1994, 1995); however, we can apply the same analysis techniques to search for shape attributes, such as concavities, within the convex hull of ORJ90. We begin with a triaxial ellipsoid approximation and use this as a reference for more complex, nonaxisymmetric shapes. Two different approaches, perturbations to an ellipsoid and successive approximations, shed light on the uncertainties of our shape models and suggest the types of shape attributes that Eros is likely to possess.

CONSTRAINTS FROM THE ECHO SPECTRAL SHAPE

The convex hull estimator considered the rotation phase dependence of the spectral edge frequencies but ignored

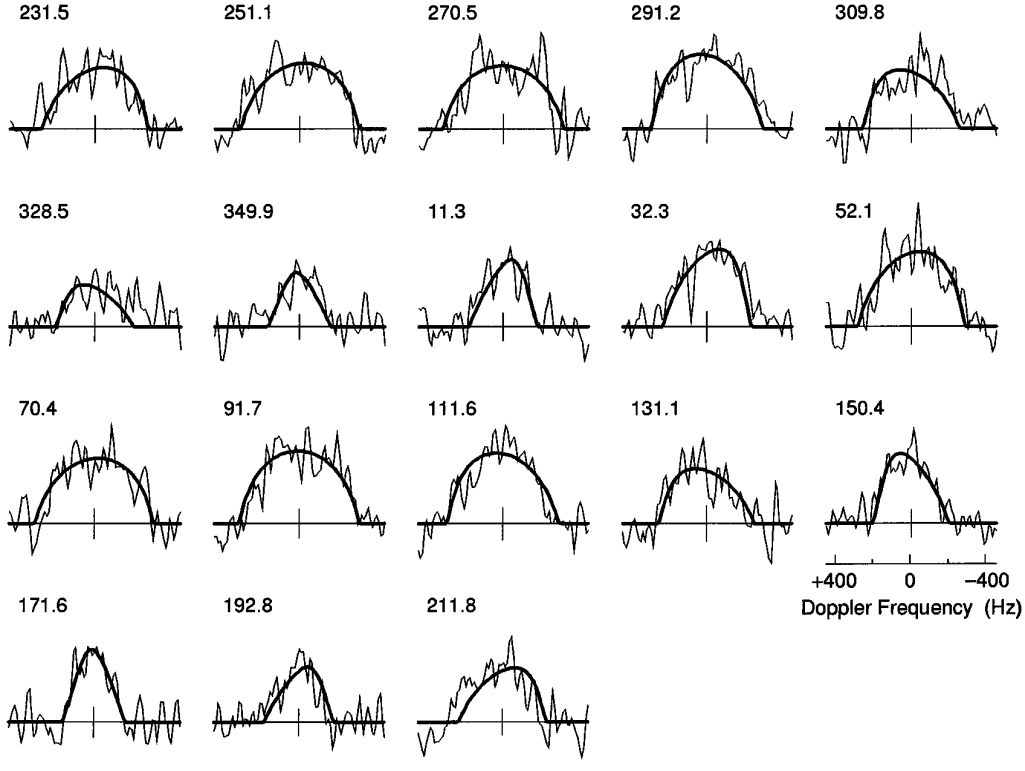

FIG. 1. Echo power is plotted on a linear scale versus Doppler frequency from +450 Hz (approaching) to −450 Hz (receding). The central bar at the origin of each spectrum shows ±1 standard deviation of the receiver noise. The data were first averaged in 20° phase bins and then smoothed to a frequency resolution of 30 Hz. The weighted-average phase is given at the upper left of each spectrum. End-on views are at 0° and 180°. The Doppler spectrum of the reference ellipsoid at each of these weighted-average phases is shown in bold for comparison with the data.

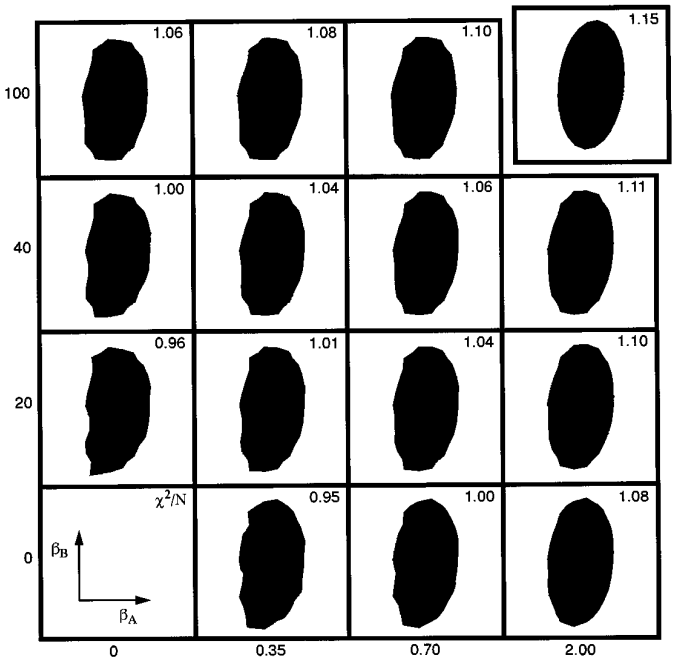

FIG. 2. The model's pole-on silhouette versus the penalty weights β_A and β_B. The χ^2/N statistic is given in the upper right of each panel. The locus of models with $\chi^2/N = 1$ runs diagonally from $(\beta_A, \beta_B) = (0, 40)$ to $(0.7, 0)$. For comparison, the silhouette of the reference ellipsoid is shown in the detached panel at the upper right. All silhouettes are seen from above the asteroid's south pole at zero rotation phase with the radar at the bottom.

the spectral shape and therefore ~90% of the available data. Hudson (1993) developed a technique that uses the evolution of the echo's delay/Doppler distribution as the target rotates and moves across the sky to estimate its three-dimensional shape, spin state, and radar scattering properties. This technique has been used to reconstruct the shapes of 4769 Castalia and 4179 Toutatis (Hudson and Ostro 1994, 1995). The Eros radar data obtained in 1975 are not resolved in time delay and therefore depend in a coupled way on size, spin vector, and scattering law. However, armed with external constraints on the asteroid's size and spin vector, we can use the rotational evolution of the spectra to place constraints on Eros' shape.

Ephemeris Correction

We adopt the 1975 site ephemeris used by Jurgens and Goldstein with the constant Doppler correction determined by ORJ90 from their convex hull analysis. (The variation of the Doppler prediction error during the observations was expected to be much less than the data's 2.73-Hz raw frequency resolution.) We assume that the model's spin axis coincides exactly with the data's (corrected) zero Doppler frequency.

Data Filtering

We smoothed the spectra by 20° in phase and 30 Hz in frequency, which is the optimal phase/frequency filter for the convex hull analysis. This choice of data filtering effectively limits the model's maximum spatial resolution. Given the data's SNR and our model results (below), it is unlikely that we have "filtered out" any significant shape information contained in the data. The phase smoothing averages data from several days during which Eros' sky coordinates changed by about 4°. This motion results in a synodic spin period of 5.2689 hr (Dunlap 1976) but does not affect the subradar latitude. Each of the 18 smoothed spectra is multiplied by a factor to permit the recalibration of its brightness scale. Thus, only the *shapes* of the spectra are used to constrain the model.

Definition of a Reference Ellipsoid

A uniform-density, triaxial ellipsoid is a useful first approximation. We adopt a body-fixed coordinate system, with origin at the ellipsoid's center of mass and axes (x, y, z) that correspond to the principal axes of smallest, intermediate, and largest moment of inertia. The ellipsoid rotates about the z-axis, which points in a direction with ecliptic coordinates of 22° longitude and +9° latitude (Taylor 1985). All of the post-1975 pole estimates predict that the target-centered declination of the radar during the 1975 Goldstone observations was within ~10° of zero, so our choice of pole direction is not critical.

Zero rotation phase is defined to occur in the observatory-based frame on 1975 January 23.34758, an epoch when the convex hull's minimum dimension appeared from the Earth to be normal to the line of sight with the longest (flat) side on the receding limb (ORJ90). (Correcting for light travel time, this orientation occurs about 76 sec earlier in the asteroid's frame.) Since this zero-phase epoch is based on the convex hull analysis, it need not correspond precisely to a time when the ellipsoid's x-axis is along the line of sight. Therefore, we define the parameter φ to be the angle between the x-axis and the plane defined by the z-axis and the line of sight at the zero-phase epoch.

We adopt an empirical radar scattering law given by $\sigma_o(\theta) = \rho \cos^n(\theta)$, where θ is the angle between the local surface normal and the line of sight, ρ is the normal reflectivity, and n is a measure of specularity (Mitchell *et al.* 1996). We assume Lambertian scattering ($n = 2$), which is slightly more diffuse than scattering laws estimated for Castalia ($n = 2.8$) and Toutatis ($n = 2.3$) (Hudson and Ostro 1994, 1995), which have circular polarization ratios similar to that of Eros ($\mu_C \sim 0.3$; JG76).

Since the subradar latitude during the 1975 observations was within 10° of the equator, and since the spectra are resolved only in Doppler frequency, there are correlations between the axis dimensions and the scattering law param-

eters, as noted by JG76. Consequently, we adopt long and intermediate dimensions for the ellipsoid from the convex hull ($2a = 34.7; 2b = 17.4$ km). With these assumed equatorial dimensions and a Lambertian scattering law, we search for the ellipsoid's polar dimension ($2c$), the angle φ, and the 18 brightness calibration factors. Using a least-squares approach, we find $2c = 14$ km and $\varphi = 6°$. The brightness calibration factors are within ~30% of unity. This model constitutes the *reference ellipsoid.*

The Doppler spectra of the reference ellipsoid provide a good first approximation to the data (Fig. 1), with $\chi^2/N = 1.15$, where N is the number of data points. With a Lambertian scattering law, the model appears limb-darkened to the radar. The Doppler spectra of the reference ellipsoid are thus asymmetric at all rotation phases other than end-on and broadside orientations. This effect alone is sufficient to explain asymmetries observed at rotation phases near 0°. However, the asymmetry near 180° is much larger, indicating shortcomings in the ellipsoid model.

In the next two sections, we explore two different approaches to extracting shape information from the Goldstone radar data. A nearly equatorial view, modest SNR, and the lack of delay-resolved echoes preclude the determination of a unique, three-dimensional shape; however, our ability to resolve the echoes in frequency and rotation phase provide sufficient geometric leverage to search for shape attributes "inside" the convex hull of ORJ90. Is there any significance to the fact that the hull's centers of figure and rotation are not aligned? What causes the spectral asymmetry near rotation phases of 180°?

METHOD 1: PERTURBATIONS TO THE REFERENCE ELLIPSOID

In this approach, we search for the minimum deviations from the reference ellipsoid that can reduce χ^2/N from 1.15 to unity. We begin by approximating the reference ellipsoid's surface with 508 triangular facets defined by 256 vertices. Each vertex is defined by a base point (**B**) and a unit direction vector (**D**). Initially, all the base points lie on the surface of the reference ellipsoid, and the direction vector at each base point is the local surface normal. Deviations from the reference ellipsoid are parameterized by 256 scalars (r), which form the first part of a parameter vector **p**.

A vertex of the perturbed shape is given by:

$$\begin{aligned} \mathbf{B} &= \mathbf{B}_E + r \cdot \mathbf{D}_E \\ \mathbf{D} &= \mathbf{D}_E \end{aligned} \tag{1}$$

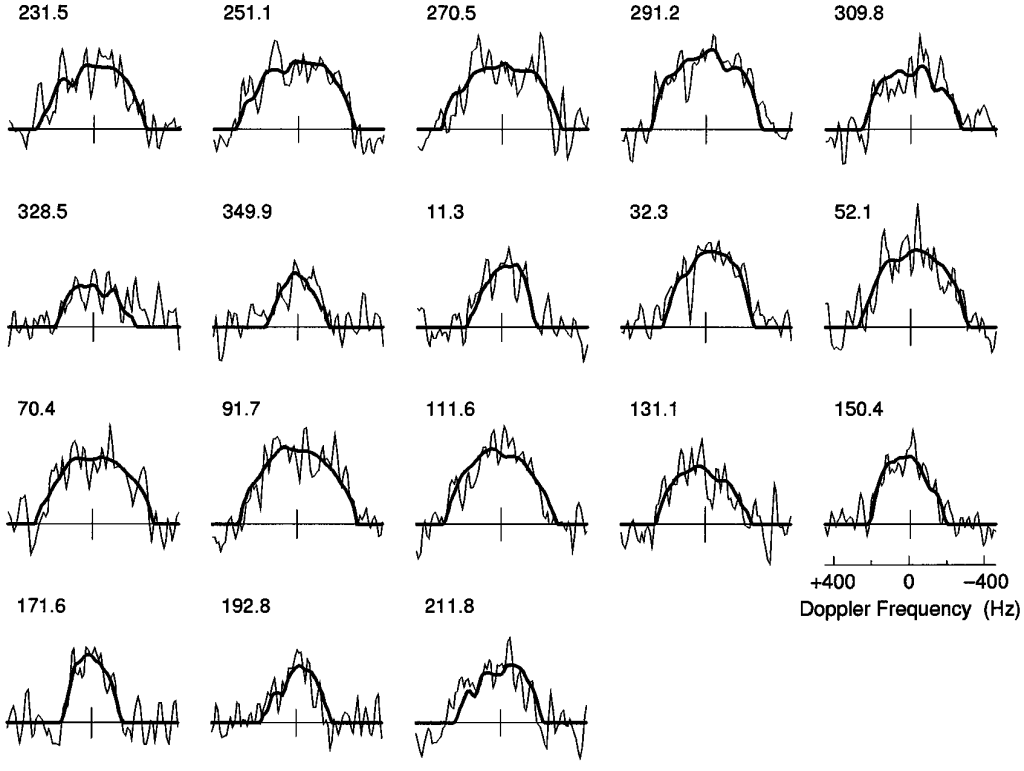

FIG. 3. The Doppler spectra of Model 1 compared with the data (see caption to Fig. 1). The greatest improvement in the spectral fit occurs at rotation phases from 210° to 310°, corresponding to views of the M1 side (see Fig. 6).

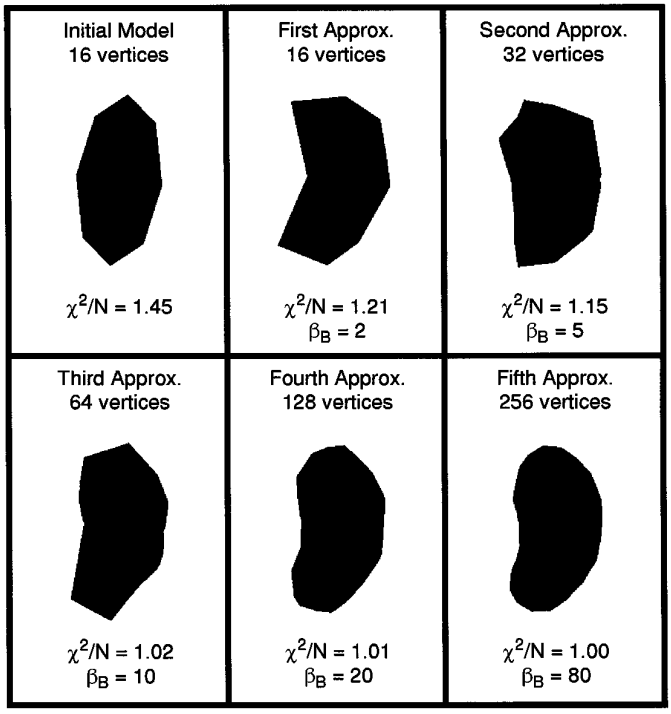

FIG. 4. Pole-on silhouettes of successive approximations to Eros' shape. All silhouettes are seen from above the asteroid's south pole at zero rotation phase with the radar at the bottom. With just 16 vertices, the gross features of the final model are already apparent.

where $\mathbf{B}_E$ and $\mathbf{D}_E$ are a base point and a direction vector of the reference ellipsoid. The rest of the parameter vector consists of 18 brightness calibration factors and the angle φ for a total of 275 free parameters. The parameter vector $\mathbf{p}$ is adjusted by minimizing an objective function $Q(\mathbf{p})$ using Powell's method (see Press *et al.* 1988). The objective function is the sum of χ^2 (the weighted sum of squared residuals) and penalty functions, which are used to impose dynamical and shape constraints.

Dynamical penalties are applied to force the shape to be consistent with a uniform-density, principal-axis rotator. With the reference ellipsoid as the starting point, the dynamical penalty weights are set high enough so that as the model's shape is perturbed away from the ellipsoid, its centroid remains close to the origin of the body-fixed coordinate system and its principal axes of inertia remain nearly aligned with the x, y, and z axes. Eros' rotation period is short enough so that the asteroid should be in principal-axis rotation (Harris 1994, Burns and Safranov 1973), so the dynamical penalty functions restrict our attention to only those perturbations that result in dynamically plausible models.

Two shape penalty functions are used to limit deviations from the reference ellipsoid and to suppress sharp angles between adjacent facets. The first is a weighting factor (β_A) times the mean value of r^2, and the second is a weighting factor (β_B) times the mean value of $\sin^2(\alpha/2)$, where α is the angle between two adjacent facets. When $\alpha = 0$, the adjacent facets are coplanar.

Figure 2 shows the pole-on silhouettes of the shapes that minimize $Q(\mathbf{p})$ for selected values of β_A and β_B. Large values of β_A force the shape toward the reference ellipsoid, for which $\chi^2/N = 1.15$, while large values of β_B drive the shape toward a sphere and $\chi^2/N > 1.15$. When β_A and β_B are small, the estimator has enough freedom to attain values of χ^2/N less than unity.

The values of χ^2/N given in Fig. 2 sample a χ^2 surface, which is a smooth, sloping function of β_A and β_B. A curve on the surface is defined by $\chi^2/N = 1$. Starting from a point on this curve and moving in a direction of decreasing β_A and β_B results in $\chi^2/N < 1$, indicating that the estimator is beginning to "fit the noise." Thus, we take models along the $\chi^2/N = 1$ curve to bound the region of acceptable deviations from the reference ellipsoid. Although we cannot define a "best-fit" shape, this procedure helps to identify the kinds of perturbations to the reference ellipsoid that can account for the asymmetries observed in the Doppler spectra.

Induced Model Symmetries

A more subtle consequence of the penalty functions is their influence on the north/south *symmetry* of the model as a result of the north/south *ambiguity* of the data. Since the subradar latitude is very near the equator, the north/south ambiguity cannot be resolved with the geometric leverage afforded by the asteroid's rotation. Thus, in attempting to fit a given feature of the Doppler spectra, our estimator is free to perturb northern vertices or southern vertices or both. Since the shape penalty functions depend on higher than linear powers of r, smaller values of Q can generally be attained by distributing a perturbation evenly among northern and southern vertices, thus imposing a degree of north/south symmetry in the model.

Symmetries can also be induced by the dynamical penalty functions. As vertices are perturbed on one side of the asteroid to improve the spectral fit near one rotation phase, there must be associated perturbations elsewhere to maintain principal axis rotation about the origin in a manner that does not compromise the goodness of fit at other rotation phases. Such " balancing" perturbations can be quite distributed but can induce a degree of symmetry. The data's low SNR does not provide much leverage in preventing such artifacts; however, the shape penalty functions are effective in suppressing features that do not play a significant role in reducing χ^2/N.

Selection of a Working Model

Deviations from the reference ellipsoid as a function of β_A and β_B are readily seen in the model's pole-on silhouette

(Fig. 2). As β_A decreases from 2 to 0, concavities begin to form on one of the long sides as the convex envelope of that side flattens. Meanwhile, the opposing long side remains highly convex. As β_B increases from 0 to 100, concavities are filled in, and the model's ends become more rounded. At $\beta_B = 100$ the model's ends are slightly more rounded than those of the reference ellipsoid. Models with $\chi^2/N = 1$ are quite similar for widely ranging combinations of β_A and β_B, which reflects the influence of the data in defining deviations from the reference ellipsoid subject to the imposed dynamical constraints. Although we cannot define a "best-fit" model, we adopt a working model with $(\beta_A, \beta_B) = (0.35, 20)$ and $\chi^2/N = 1$ (Fig. 3). We will henceforth refer to this as Model 1.

METHOD 2: SUCCESSIVE APPROXIMATIONS (VERTEX DOUBLING)

In this approach, we begin with a polyhedral approximation to the reference ellipsoid consisting of 28 triangular facets defined by 16 vertices. Dynamical and shape penalty functions are used as before, except that β_A is fixed at zero—that is, there is no penalty associated with deviations from the reference ellipsoid. Even after $Q(\mathbf{p})$ has been minimized for this 16-vertex model, χ^2/N is larger than that of the *ideal* reference ellipsoid. Evidently, 16 shape parameters (as opposed to only three for the reference ellipsoid) are insufficient to produce a polyhedral model that is superior to the reference ellipsoid, even though some gross features of the shape are beginning to emerge.

Next, we resample the shape that results from minimizing $Q(\mathbf{p})$ for the 16-vertex model with twice the number of vertices, as follows. The new model is initialized with six base points placed on the previous model's surface where it intersects the $\pm x$, $\pm y$, and $\pm z$ axes. These base points define $(2 \times 6) - 4 = 8$ triangular facets. A new base point is placed at the midpoint of the longest facet side and then moved radially until it lies on the previous model's surface. This procedure is repeated until the desired number of base points have been obtained. The resampled shape is thus defined by more or less equidistant base points, and hence roughly equal-area facets. A triaxial ellipsoid is fit to the new collection of base points, and for each base point we find the point on the ellipsoid's surface such that the base point lies along the surface normal when viewed from that point. The unit direction vector $(\mathbf{D})$ for the base point is then set to be that normal. Then, $Q(\mathbf{p})$ is minimized for the new parameter vector. This process is repeated until the desired accuracy is achieved.

Figure 4 shows the pole-on silhouettes of the successive

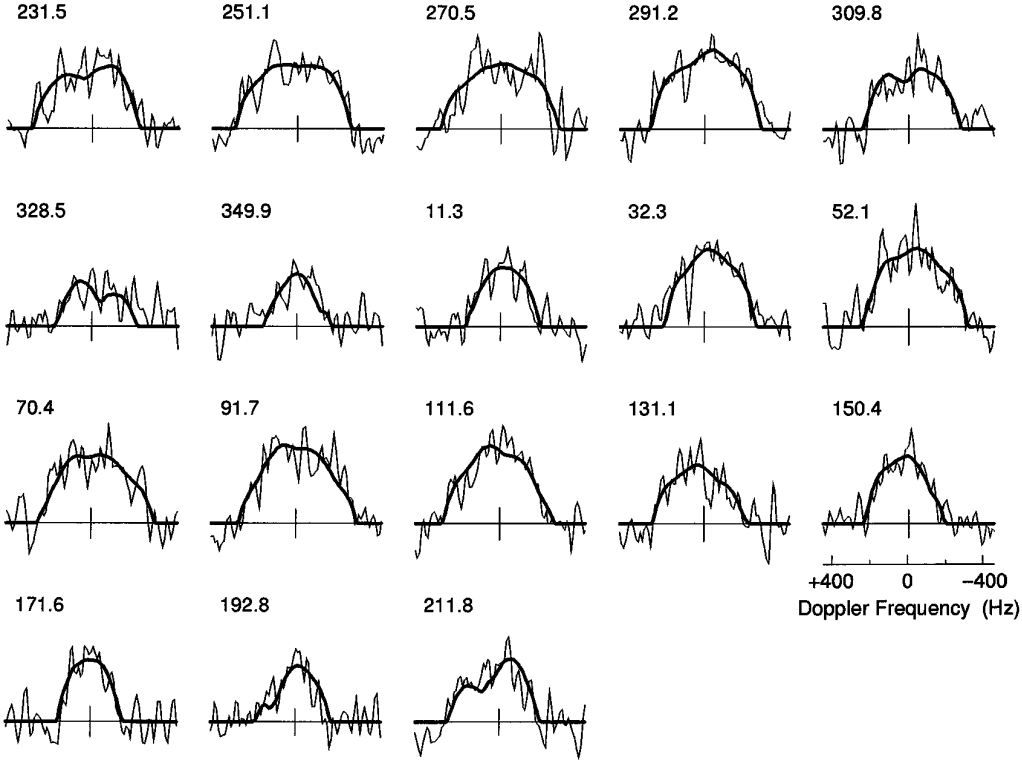

FIG. 5. The Doppler spectra of Model 2 compared with the data (see caption to Fig. 1). The greatest improvement in the spectral fit occurs at rotation phases from 210° to 310°, corresponding to views of the M1 side (see Fig. 6).

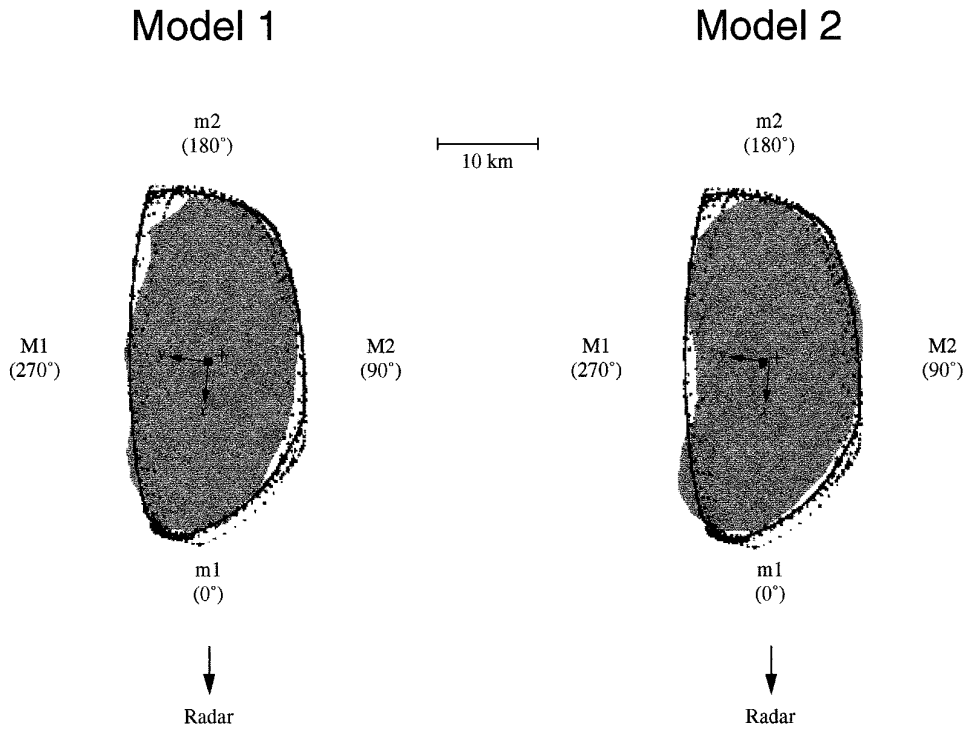

FIG. 6. Pole-on silhouettes of Models 1 and 2 compared with the convex hull of ORJ90. The silhouettes and hull are viewed from above the asteroid's south pole at zero rotation phase with the radar toward the bottom. Each silhouette has been aligned with the hull by eye. Coordinate axes are drawn to radiate from each model's center of mass. The hull's center of figure is shown by the black square and its center of rotation is indicated by a "+" symbol. Approximate locations of lightcurve extrema (see Table I) are indicated around the hull's perimeter (see ORJ90 for precise locations).

approximations to Eros' shape. With just 16 vertices, our estimator searches for gross shape attributes as it minimizes $Q(\mathbf{p})$. As vertices are added, the shape is refined. Very little improvement is achieved by doubling the number of vertices from 128 to 256, indicating convergence. Note that β_B increases as vertices are added, because the average angle between adjacent facets can be smaller, and larger values of β_B are required to suppress insignificant (typically small-scale) features. For the final 256-vertex model (Model 2), β_B has been adjusted to yield $\chi^2/N = 1$ (Fig. 5) at the minimum of $Q(\mathbf{p})$.

COMPARISON OF MODELS 1 AND 2

The two approaches outlined above yield distinct shapes. Model 1 exhibits several features (concavities and ridges) along one side, whereas Model 2 has a single large concavity along the same side and a smoother, more rounded appearance. What can we learn about Eros' shape from these two models? Their dissimilarity is one measure of our limited ability to constrain Eros' shape with the available radar data. Nevertheless, both models share some attributes. By a careful consideration of how each model attempts to improve the spectral fit, we can identify the types of features that Eros is likely to possess. We begin this section by comparing the pole-on silhouettes of Models 1 and 2 with the convex hull of ORJ90. There is reasonable agreement between these very different approaches to modeling the radar data. Following this is a detailed comparison of Models 1 and 2, where we show that each model accounts for the observed spectral asymmetries in basically the same way.

Pole-on Silhouette

Rotational variation of the echo bandwidth influences the convex hull and the pole-on silhouette of the three-dimensional shape in a similar manner. Both approaches seek to confine Eros' extent orthogonal to the spin axis such that the echo power becomes much less than the noise level near the Doppler frequencies of the apparent spectral edges. (Our ability to detect echoes from the target's *limbs* depends on the scattering law and the data's SNR.) The convex hull approach does this directly through the use of a spectral edge estimator, whereas three-dimensional shape reconstruction does this indirectly as $Q(\mathbf{p})$ is minimized.

Figure 6 compares the pole-on silhouettes of Models 1 and 2 with the convex hull of ORJ90. To produce each

overlay, the silhouette and the hull were first rotated to their orientations at the zero-phase epoch (with the radar toward the bottom), and then the translational alignment was adjusted by eye. Coordinate axes are drawn to radiate from each model's center of mass. The "camera" is above the south pole, and each model's x-axis points roughly 5° clockwise from the radar-facing direction. The hull's center of figure is shown by a black square, and its center of rotation is identified by a "+" symbol. If there were no errors in any of the estimations, then the hull would appear to wrap around each model's pole-on silhouette like a tightly stretched rubber band when the hull's center of rotation coincided with the model's center of mass.

Imperfect agreement between the silhouettes and the hull is not unexpected, given the data's noise level. Model 1 shows somewhat better agreement with the dotted hull profiles, which provide an estimate of the nominal hull's uncertainty (ORJ90). Model 2 tends to have larger radii of curvature than the nominal hull, especially at the ends. These discrepancies probably result from our use of penalty functions, which suppress sharp angles between facets for both models and departures from the (smooth) reference ellipsoid for Model 1. The trade-off between producing a smooth model and accurately fitting the spectral edges may account for some of φ's offset from zero in both models. In addition, φ might differ from zero since the principal axes of inertia need not be aligned with the maximum and minimum radii of either model's pole-on silhouette.

Concavities, Tapering, and Bends

The upper half of Fig. 7 shows a map of the deviation scalars (r) for Model 1. The model exhibits a pattern of alternating ridges and troughs, which is much more prominent on the M1 side than on the M2 side. The most prominent concavity is centered near 300° longitude, and a second concavity is centered near 240°. The depression at the m2 end is nearly surrounded by a ring of positive deviations—that is, the m2 end has a larger radius of curvature than the ends of the reference ellipsoid. Positive deviations from 320° to 360° and opposing negative deviations centered near 20° define a bend of the m1 end with respect to the x-axis.

The high degree of north/south symmetry is an artifact of our approach to modeling the north/south ambiguous data, as described above. There are also symmetries about the x–z plane.[1] The subdued ridge at 60° opposes the concavity at 300°, while the subdued trough at 90° opposes the ridge at 270°. This ridge/trough pair on the M2 side is barely noticeable in the pole-on silhouette (Fig. 2) and does not play an obvious role in improving the spectral fit.

[1] The x–z plane would project onto Fig. 7 as vertical lines at 0° and 180°.

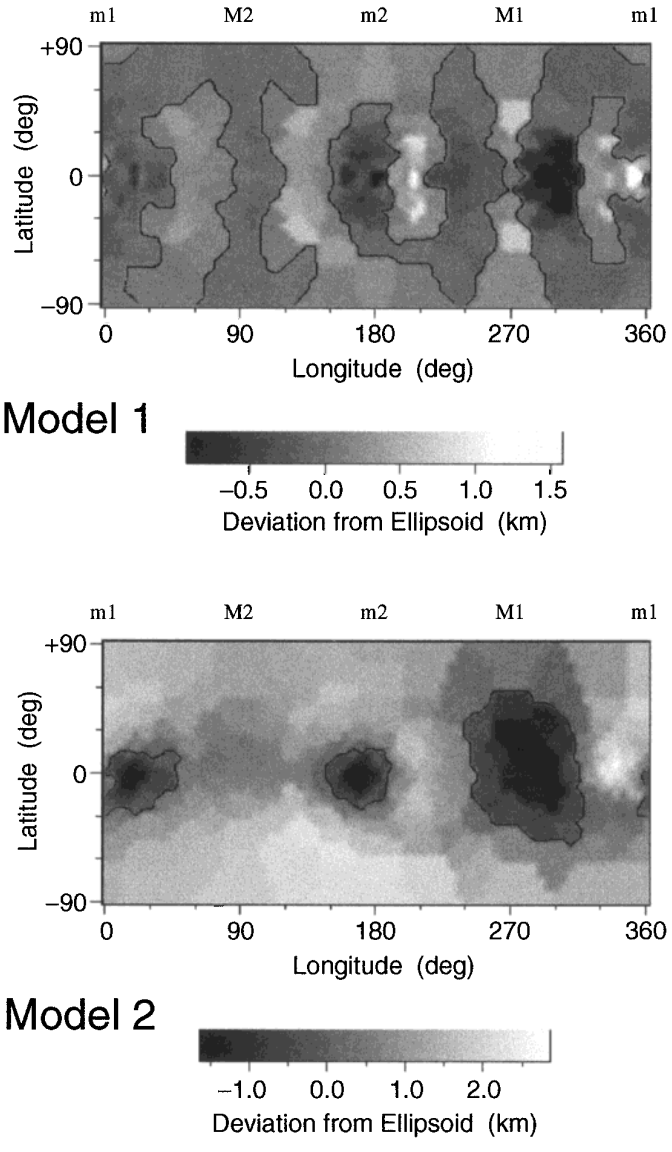

FIG. 7. Map of deviation scalars (r) for Models 1 and 2 shown in rectangular projections of target-centered longitude and latitude, which are defined with respect to the body-fixed, principal-axis coordinate system. Longitude increases opposite to the sense of rotation such that the longitude of the sub-radar point leads rotation phase by the angle φ, which is about 5° for both models. The approximate target-centered longitudes of the Earth during lightcurve extrema are indicated along the top (M1 = Max 1, M2 = Max 2, m1 = min 1, m2 = min 2). The $r = 0$ contour is drawn for clarity.

Thus, we cannot rule out the possibility that some of the subdued structure on the M2 side arises from "balancing" perturbations, which are an expected consequence of the dynamical penalty functions.

The lower half of Fig. 7 shows a map of deviation scalars (r) for Model 2. The deviations are relative to the ideal reference ellipsoid along normals to that ellipsoid's surface.

There are fewer and larger deviations in Model 2; however, they show some correspondence to the deviations in Model 1. For example, the large concavity from 240° to 320° longitude in Model 2 is in roughly the same location as the trough-ridge-trough pattern centered at 270° in Model 1. In addition, both models have a rounded m2 end and a bend in the m1 end, which is especially prominent in Model 2.

Symmetries in Model 2 are much less pronounced than those in Model 1. The pattern of alternating ridges and troughs is virtually absent, and the north/south symmetry is also greatly reduced, although deviations remain centered roughly about the model's "equator." The comparative weakness of symmetries in Model 2 probably results from the successive approximation approach, which places less weight on the reference ellipsoid as an initial condition, and the fact that β_A is set to zero, thereby eliminating one of the causes of north/south symmetries.

Both models account for the pronounced spectral asymmetry from ~190°–210° of rotation phase by placing one or more concavities along the M1 side. As a concavity rotates into view (Fig. 8), part of its interior is tilted toward the radar and thus provides a higher radar return than the surface of an ellipsoid would at the same Doppler shift from the spin axis. In addition, each model's y–z cross section (and mass distribution) as a function of x is asymmetric about $x = 0$. The m1 end is tapered and extends about 1 km farther from the spin axis than does the rounded m2 end (see Fig. 7). This allows concavities near the m1 end to extend farther from the spin axis as they rotate into view, which enhances the spectral asymmetry.

The fact that both models account for the spectral asymmetry at rotation phases from ~190°–210° by placing one or more concavities on the asteroid's M1 side suggests that this is a real characteristic of Eros' shape. This interpretation is compatible with the "difference in surface reflectivity or surface slopes on opposite sides of the asteroid" noted by Jurgens and Goldstein (JG76) as well as the misalignment of the convex hull's centers of figure and rotation (ORJ90). Comparing Models 1 and 2, we cannot say whether a single large concavity or several smaller ones are responsible for the observed spectral asymmetry. Furthermore, the data's north/south ambiguity combined with an equatorial view precludes the determination of the

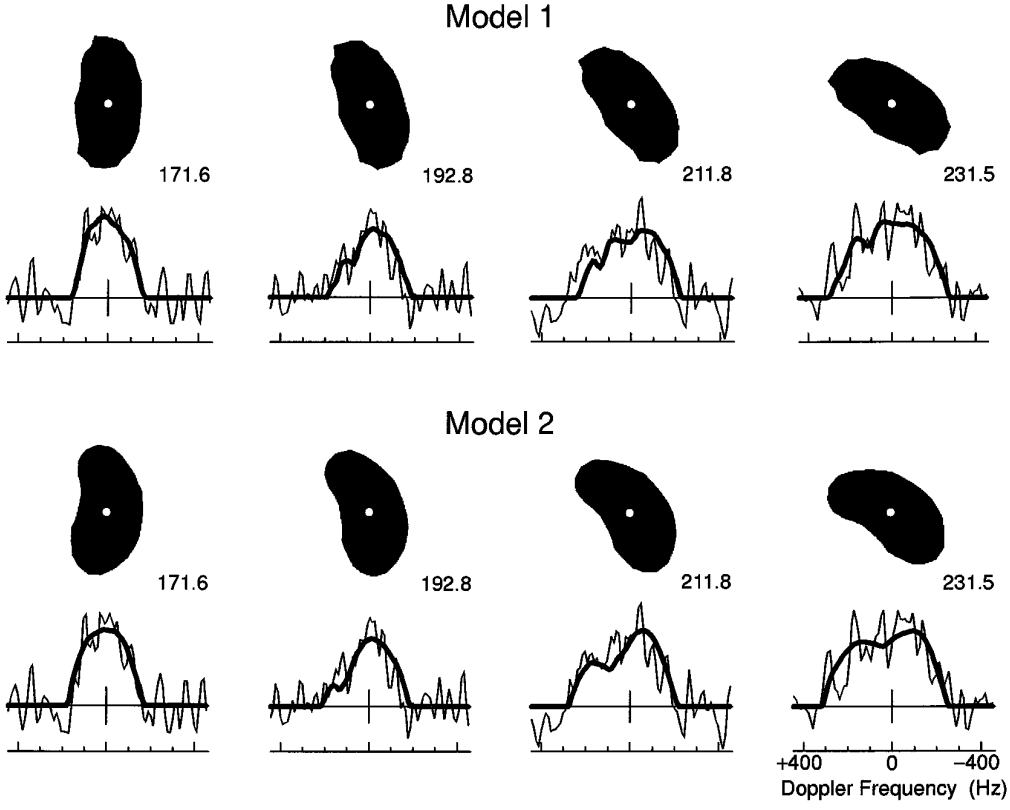

FIG. 8. Comparison of the Doppler spectra of Models 1 and 2 with the data at four nearby rotation phases. Above each spectrum is the model's pole-on silhouette as seen from the *north* pole with the radar toward the bottom. Each silhouette is drawn at the same scale as the Doppler frequency axis and at the indicated rotation phase. The Doppler spectra can be thought of as scans of radar brightness in the plane of the sky taken through a slit parallel to the target's projected spin vector.

TABLE I
Shape and Mineralogy

MP96 phase[a]	Inferred mineralogy[b]	Lightcurve extremum[c]	ORJ90 phase[d]	View of Eros[e]
=0		Min 2	~180	m2: rounded end
~90	px-rich	Max 1	~270	M1: long side with concavities
~180		Min 1	~0	m1: bent, tapered end
~270	ol-rich	Max 2	~90	M2: highly convex side

[a] Rotation phase as defined by Murchie and Pieters (1996), where zero degrees corresponds exactly to Min 2. The rotation phases of other lightcurve extrema are approximate.

[b] Eros' average visual/infrared spectrum is classified as S-IV in the system of Gaffey *et al.* (1993). The relatively px-rich (ol-rich) side corresponds to MP96 phases of 320°–170° (170°–320°).

[c] Lightcurve extrema as defined by Millis *et al.* (1976).

[d] Approximate rotation phase of ORJ90. See Fig. 6 of ORJ90 for precise phases of lightcurve extrema.

[e] See Figs. 6 and 7.

three-dimensional shape of any of these concavities, which would help to clarify whether they are craters, troughs, or bends in Eros' overall shape. In any event, the topography of the M1 side is apparently much more dramatic than that of the M2 side.

The pole-on silhouette of Model 2 looks like a kidney bean, which resembles a nearly pole-on optical image derived from speckle interferometry (Drummond and Hege 1989). The speckle image is based on data obtained in December, 1981, when the target-centered declination of the Earth was probably between −55° and −75°. The similarity between the speckle image and Model 2 is suggestive, given that the two experimental techniques are completely independent. However, the uncertainties are sufficiently large that we cannot rule out a shape more similar to Model 1.

SHAPE AND MINERALOGY

Visual and infrared observations establish Eros as an S-class asteroid (Chapman *et al.* 1975, Tholen 1989). Recently, Murchie and Pieters (1996) reanalyzed visual/infrared spectra that were acquired in January, 1975, at nearly the same time of the Goldstone radar observations. They found that Eros' average spectrum falls within the S-IV subgroup in the classification system of Gaffey *et al.* (1993) but that the spectrum varies with rotation phase. Murchie and Pieters identified two sides of Eros, each spanning ~180° of rotation phase. Both sides fall within the S-IV group, but one side has a higher olivine/pyroxene ratio than the opposite side.

According to Murchie and Pieters, such mineralogical variations could be interpreted in different ways. Eros could be an intact fragment from a (highly or slightly) differentiated parent body, in which case mineralogical variations in that body might be preserved in Eros. Alternatively, Eros could be a ''rubble pile'' consisting of fragments from one or more parent bodies, and the relative locations of mineralogically distinct units could be random.

Table I shows the correspondence between the mineralogical variations and our shape models. Eros' px-rich side is marked by one or more prominent concavities, while the ol-rich side lacks such features. We do not have sufficient information to determine the exact shapes of the concavities, much less their origin. The concavities on the M1 side of Model 1 could plausibly be impact features; however, the large M1 concavity of Model 2 could just as plausibly define a bend in Eros' shape. Thus, specific geologic interpretations for Eros' shape and mineralogy await NEAR's rendezvous in 1999.

ACKNOWLEDGMENTS

We are grateful for thoughtful reviews by S. Murchie and an anonymous referee. The research described in this paper was carried out by the Jet Propulsion Laboratory, California Institute of Technology, and was sponsored by Washington State University through an agreement with the National Aeronautics and Space Administration.

REFERENCES

Asphaug, E., J. M. Moore, D. Morrison, W. Benz, M. C. Nolan, and R. J. Sullivan 1996. Mechanical and geological effects of impact cratering on Ida. *Icarus* **120,** 158–184.

Burns, J. A., and V. S. Safranov 1973. Asteroid nutation angles. *Mon. Not. R. Astron. Soc.* **165,** 403–411.

Chapman, C. R., D. Morrison, and B. Zellner 1975. Surface properties of asteroids: A synthesis of polarimetry, radiometry, and spectrophotometry. *Icarus* **25,** 104–130.

Drummond, J. D., and E. K. Hege 1989. Speckle interferometry of asteroids. In *Asteroids II* (R. P. Binzel, T. Gehrels, and M. S. Matthews, Eds.), pp. 171–191. Univ. of Arizona Press, Tucson.

Dunlap, J. L. 1976. Lightcurves and the axis of rotation of 433 Eros. *Icarus* **28,** 69–78.

Gaffey, M., J. Bell, R. Brown, T. Burbine, J. Piatek, K. Reed, and D. Chaky 1993. Mineralogic variations within the S-type asteroid class. *Icarus* **106,** 573–602.

Geissler, P., J.-M. Petit, D. D. Durda, R. Greenberg, W. F. Bottke, and M. C. Nolan 1996. Erosion and ejecta reaccretion on 243 Ida and its moon. *Icarus* **120,** 140–157.

Greenberg, R., M. C. Nolan, W. F. Bottke, Jr., R. Kolvoord, and J. Veverka 1994. Collisional history of Gaspra. *Icarus* **107,** 84–97.

Harris, A. W. 1994. Tumbling asteroids. *Icarus* **107,** 209–211.

Hudson, R. S. 1993. Three-dimensional reconstruction of asteroids from radar observations. *Remote Sensing Rev.* **8,** 195–203.

Hudson, R. S., and S. J. Ostro 1994. Shape of asteroid 4769 Castalia (1989 PB) from inversion of radar images. *Science* **263,** 940–943.

Hudson, R. S., and S. J. Ostro 1995. Shape and non-principal axis spin state of asteroid 4179 Toutatis. *Science* **270,** 84–86.

Jurgens, R. F., and R. M. Goldstein 1976. Radar observations at 3.5 and 12.6 cm wavelength of asteroid 433 Eros. *Icarus* **28,** 1–15.

Magnusson, P. 1989. Pole determinations of asteroids. In *Asteroids II* (R. P. Binzel, T. Gehrels, and M. S. Matthews, Eds.), pp. 1180–1190. Univ. of Arizona Press, Tucson.

Millis, R. L., E. Bowell, and D. T. Thompson 1976. UBV photometry of asteroid 433 Eros. *Icarus* **28,** 53–67.

Mitchell, D. L., S. J. Ostro, R. S. Hudson, K. D. Rosema, D. B. Campbell, R. Veléz, J. F. Chandler, I. I. Shapiro, J. D. Giorgini, and D. K. Yeomans 1996. Radar observations of asteroids 1 Ceres, 2 Pallas, and 4 Vesta. *Icarus* **124,** 113–133.

Murchie, S. L., and C. M. Pieters 1996. Spectral properties and rotational spectral heterogeneity of 433 Eros. *J. Geophys. Res.* **101** (No. E1), 2201–2214.

Ostro, S. J., K. D. Rosema, and R. F. Jurgens 1990. The shape of Eros. *Icarus* **84,** 334–351.

Ostro, S. J., K. D. Rosema, R. S. Hudson, R. F. Jurgens, J. D. Giorgini, R. Winkler, D. K. Yeomans, D. Choate, R. Rose, M. A. Slade, S. D. Howard, and D. L. Mitchell 1995. Extreme elongation of asteroid 1620 Geographos from radar images. *Nature* **375,** 474–477.

Press, W. H., B. P. Flannery, S. A. Teukolsky, and W. T. Vetterling 1988. *Numerical Recipes in C,* Chap. 10, pp. 309–317. Cambridge Univ. Press, Cambridge, UK.

Santo, A. G., S. C. Lee, and R. E. Gold 1995. NEAR spacecraft and instrumentation. *J. Astron. Sci.* **43** (No. 4), 373–397.

Scheeres, D. J., S. J. Ostro, R. S. Hudson, and R. A. Werner 1996. Orbits close to asteroid 4769 Castalia. *Icarus* **121,** 67–87.

Taylor, R. C. 1985. The pole orientation of asteroid 433 Eros determined by photometric astrometry. *Icarus* **61,** 490–496.

Tholen, D. J. 1989. Asteroid taxonomic classifications. In *Asteroids II (*R. P. Binzel, T. Gehrels, and M. S. Matthews, Eds.), pp. 1139–1150. Univ. of Arizona Press, Tucson.

Zellner, B. 1975. New findings about Eros. *Sky and Telescope* (December 1975), pp. 376–379.

Zellner, B. 1976. Physical properties of asteroid 433 Eros. *Icarus* **28,** 149–153.